



# Microstructure and mechanical performance of flat resistance element welded aluminum alloy/Q235 steel joints

Liangyu Fei<sup>1</sup> · Shengdun Zhao<sup>1</sup> · Peng Zhang<sup>1</sup> · Zhiyan Feng<sup>1</sup> · Fei Jiang<sup>1</sup> · Hao Zhou<sup>1</sup>

Received: 15 October 2021 / Accepted: 22 March 2022 / Published online: 8 April 2022

© The Author(s), under exclusive licence to Springer-Verlag London Ltd., part of Springer Nature 2022, corrected publication 2022

## Abstract

Among recently developed joining technologies, resistance element welding (REW) is an effective process for joining hybrid materials. In this study, Al alloy/Q235 steel joints were produced via a flat REW (FREW) technique. The FREW joint was lighter than the traditional REW joint, and no bulges existed on the surface of the specimen. The process was performed using two methods with different positions of sheets and rivets: upward FREW (UFREW) and downward FREW (DFREW). The microstructure and tensile shear performance of the joints obtained via FREW were investigated. The maximum peak tensile shear loads of the UFREW and DFREW joints were 5537 N and 5656 N, respectively; and their maximum energy absorption values were 20.98 J and 16.55 J, respectively. The failure mode of the FREW joints changed from interface failure, to pull-out, and then to base material pull-out modes with an increase in welding current.

**Keywords** Flat resistance element welding · Hybrid material joining · Microstructure · Tensile shear performance · Failure mode transition

## 1 Introduction

With the environmental issues brought about by global warming, the greening and lightweighting of automobiles have become a major trend. To meet the cost and performance requirements of body manufacturing while maintaining lightweight, the choice of hybrid materials such as Al and steel has become mainstream [1].

Various material weld bonding processes have been developed, including ultrasonic spot welding [2], tungsten inert gas spot welding [3], and friction stir welding [4]. Among these processes, resistance welding is widely used in the manufacture of steel vehicle bodies due to its low price, high efficiency, and high automation level [5]. Pouranvari and Marashi [6] that approximately 2000–5000 spot welds exist in a modern vehicle. However we cannot obtain reliable Al and steel joints via resistance welding, due to the high thermal conductivity, high coefficient of linear expansion of Al and low solid solution between Al and steel [7]. The resistance spot welding of Al and steel results in brazed

joints at the interface, producing brittle Al-Fe intermetallic compounds at the joints [8].

For the cold forming method of joining, current promising processes include clinching and self-pierce riveting (SPR). SPR has been widely used because of its high fatigue strength; moreover, it does not require predrilling, and does not produce fumes. Xu [9] investigated the effects of die type, plate thickness combination, and rivet length on joint strength. They reported that longer rivets enable higher interlocking of joints but reduce bottom thickness; moreover, different plate thickness combinations also affect the interlocking of plates and bottom thickness. Ma et al. [10] investigated the effects of rivet hardness, rivet length, and die shape on the SPR performance and joint strength of Al alloy AA6061-T6 and mild steel CR4. They concluded that softer rivets can achieve a wider rivetable range, while longer rivets can achieve better tensile shear performance. However, SPR also exhibits disadvantages, such as bulges on one side of the joint, the possibility of galvanic corrosion between the steel rivet and the Al base material (BM), and the need for high forming forces.

In response to the difficulty of welding dissimilar materials, Meschut et al. [11] proposed a new welding method called resistance element welding (REW), which is a two-step process: (1) a hole is punched onto the Al plate, and (2)

✉ Shengdun Zhao  
sdzhao@xjtu.edu.cn

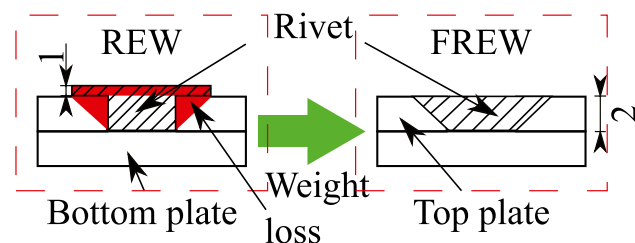
<sup>1</sup> School of Mechanical Engineering, Xi'an Jiaotong University, Xianning West Road, 710049 Xi'an, China

**Table 1** Chemical composition

Material	Nominal chemical compositions (wt.%)							
	Si	Mn	C	P	S	Fe		
Q235 steel	0.4	1.0	0.14	0.04	0.02	Balance		
Al6061	0.06	0.01	0.18	0.25	0.9	0.02	0.5	Al Balance

a steel rivet is placed into the hole on the Al plate to weld the rivet and the steel plate. They analyzed friction element welding, SPR and REW, and concluded that friction element welding and REW have small forming forces, and good application prospects. Ling et al. [12] used RSW and REW to join 6061 Al alloy/uncoated 22MnMoB. The sheet thickness of Al and steel was 2 mm and 1.8 mm, respectively. REW obtained considerably greater tensile shear load than RSW. Manladan et al. [13] joined 1.5 mm AZ31 Mg alloy and 0.7 mm 316L austenitic stainless steel by using REW, and the peak load of the joint was 3.71 kN. Schmal and Meschut [14] joined LITECOR hybrid materials (with metallic cover layers and polymer-based cores) with press-hardened steel. The determined welding current range was small and largely due to sensitivity to thermal damage of the LITECOR material. The maximum tensile shear load of the REW joints was between SPR and resistance spot shunt welded joints, which was 1.4 kN in combination with the 0.8 mm hybrid material cover sheet and 2.9 kN in combination with the 1.6 mm hybrid material cover sheet. Troschitz et al. [15] presented an approach for embedding an auxiliary unit into thermoplastic composites and joined thermoplastic composites to steel sheet by using REW. The maximum tensile shear load of the joints was 3.7 kN. Wang et al. [16] performed REW to produce Al/Ti joints. A metallurgical bond was formed between the Ti rivet and sheet, and the maximum tensile shear load was approximately 1.3–2.3 times higher than that of riveted joints.

REW can provide a strong connection for hybrid materials. However, the rivets used in this study always leave a rivet cap on the outside of the plate to secure the joints, increasing general weight and limiting the applicability of REW to a certain extent. To resolve these problems, this study analyzes and compares the microstructure and

**Fig. 1** Diagram of the REW and FREW processes

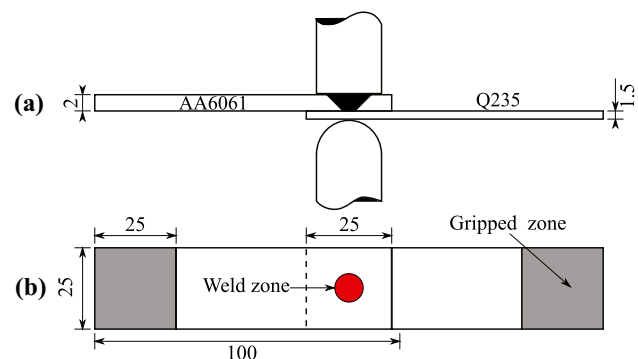
mechanical properties of joints welded using flat REW (FREW) with circular table rivets.

## 2 Materials and methods

The BMs used in this study were AA6061 Al alloy (2 mm) and Q235 steel (1.5 mm). The auxiliary unit used in FREW was a round table-shaped hot dip galvanized (HDG) Q235 rivets with a diameter of 5 mm at the bottom and 9 mm at the top. The chemical compositions of the materials used in this study are provided in Table 1. The traditional REW and FREW processes are illustrated in Fig. 1. FREW removes the rivet caps and reduces the weight of the Al plates, resulting in a weight reduction of 0.16 g per joint.

The joining process is performed using two different methods: upward FREW (UFREW) and downward FREW (DFREW), as illustrated in Figs. 2 and 3, respectively. The AA6061 and Q235 sheets used in this study for both processes were 100 mm long and 25 mm wide, and 2 mm and 1.5 mm thick, respectively. The sheets were ground with abrasive paper to remove surface oxides and cleaned with alcohol prior to welding. For UFREW and DFREW, holes were drilled into the center of the 25 mm overlapping area of the Al alloy sheets. Thereafter, rivets were placed into the corresponding holes, followed by the welding of steel sheets and rivets.

UFREW and DFREW were performed on an alternating current resistance welder, which was capable of generating a welding current of 2–22 kA. The electrode force used in this study was 3.6 kN. The electrodes were made of CuZrCr alloy.

**Fig. 2** Diagram of UFREW: (a) UFREW process and (b) tensile shear test specimen

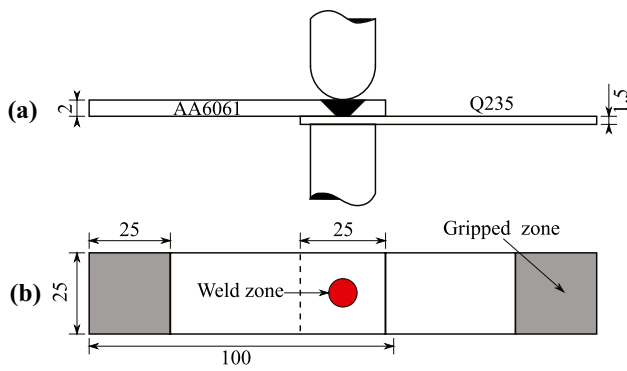


**Fig. 3** Diagram of DFREW: (a) DFREW process and (b) tensile shear test specimen

For UFREW, a spherical electrode and a flat electrode were used on the steel and the Al sides, respectively. For DFREW, the arrangement was the opposite. The process parameters used for this study were established through preliminary experiments, as indicated in Table 2.

Samples for metallographic investigation were cut from the center of the joints, mounted, ground, and polished in accordance with the standard metallographic preparation procedures. The steel and Al sides of the joints obtained by via UFREW and DFREW were etched with a 4% alcohol nitrate solution and Keller reagent, respectively.

The macrostructure of the joints was observed with a Nikon SMZ745 stereomicroscope, while the microstructure was observed using a Nikon MA200 metallographic microscope. Carl Zeiss EVO 10 and Hitachi SU3500 tungsten filament scanning electron microscopes equipped with energy-dispersive spectrometers were used to examine microstructure and interfacial properties. Hardness testing was performed using a Huayin HVT-100A Vickers microhardness tester (100 g load, 15s dwell time). Tensile shear test was performed on an Instron 5982 material testing system at a speed of 1 mm/min.

### 3 Results and discussion

#### 3.1 Macrostructures and microstructures

Figure 4a, c show the typical macroscopic morphology of a joint produced via UFREW and DFREW. Both joints have an asymmetrical nugget, with the rivet side having a larger

part because the thickness of the Q235 rivet (2 mm) is higher than that of the bottom plate (1.5 mm). A higher body resistance leads to higher heat generation at the rivet side.

At the locations indicated by the dashed line in Fig. 4a, c, Al alloys are brazed around the rivet and the steel plate. They are melted and coated onto the steel. A similar phenomenon was observed by Wan et al. [17] when performing RSW on Al6062 alloy/ HDG mild steel. They reported that due to the extremely high thermal conductivity of Al alloys, most of the heat generated at the Al/steel interface was transferred into the Al plate and the steel remained solid. As depicted in Fig. 5a, b, nuggets were only formed on the Al side with the microstructure having columnar grains oriented toward the heat diffusion direction.

The typical microstructures of the rivet/steel plate joints obtained using both processes are highly similar. From Fig. 4b, d, the microstructure of rivets can be divided into three zones: the nugget, heat-affected zone (HAZ), and BM. Figure 6a indicates that the microstructure of the nugget contains lath martensite. From the Fe-C phase diagram [18], the nugget solidifies to form  $\delta$  ferrite during the cooling process. Then, part of the solid-state  $\delta$  ferrite is transformed into  $\gamma$  austenite due to inclusion crystal reaction and completely transformed to austenite after cooling. Given to the presence of cooling water, the extremely high cooling rate resulted in the microstructure of the nugget being transformed into lath martensite [19].

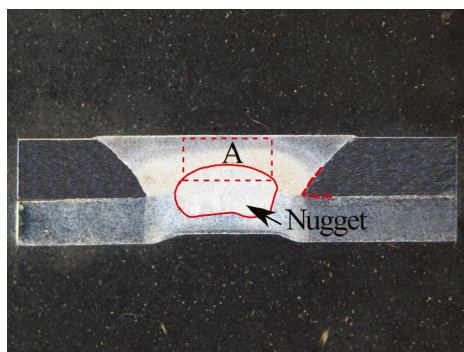
In Fig. 4b, the HAZ of the Q235 rivet of the UFREW joints is divided into two different zones: the upper-critical HAZ (UCHAZ) and the inter-critical HAZ (ICHAZ). UCHAZ can be divided into the coarse-grained and fine-grained zones (Fig. 6b, c). The peak temperature in the UCHAZ region is higher than  $A_{C3}$ , and the microstructure of the BM is fully transformed into austenite and then into martensite after cooling. Meanwhile, the coarse-grained zone forms a large grain-sized austenite due to the higher temperature. The fine-grained zone has a smaller austenite grain size, which forms larger and smaller ferrite grains after cooling. The peak temperature material in the ICHZA zone is between  $A_{C1}$  and  $A_{C3}$ , where only part of the microstructure of the BM is transformed into austenite, while the rest is transformed into allotriomorphic ferrite. Beni et al. [20] reported that austenite will transform into martensite, ferrite, and bainite upon cooling, and cooling rate makes a significant contribution to the microstructure. In this study, the microstructure of ICHAZ consists of martensite and ferrite, as shown in Fig. 6d.

The microstructure of the BM of the Q235 steel rivet for the FREW joints is shown in Fig. 7a, b, and it basically consists of ferrite and pearlite. For the FREW joints, a certain deformation of the grains is observed in the upper part of the rivet, which may be produced by the cold working of the rivet due to the electrode force. For DFREW, the relatively small contact area between the electrode and the rivet leads

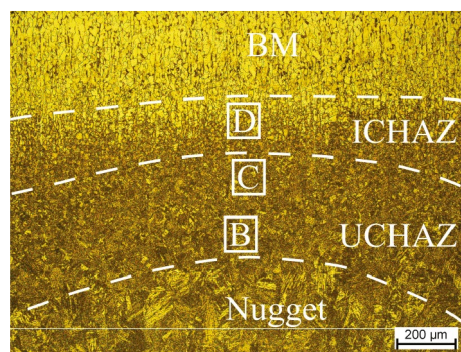
**Table 2** Welding parameters for the study

Method	Welding current (kA)	Welding time (ms)
UFREW	9–15 (in 1 kA increment)	300
DFREW	11–15 (in 1 kA increment)	300

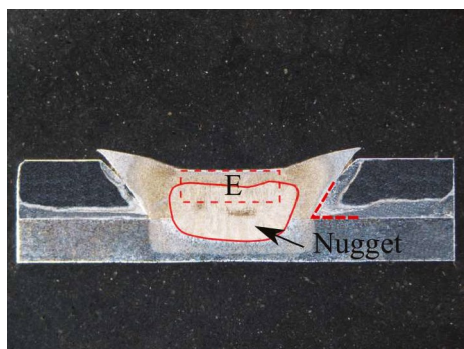
**Fig. 4** Macrostructure and microstructure of a FREW joint



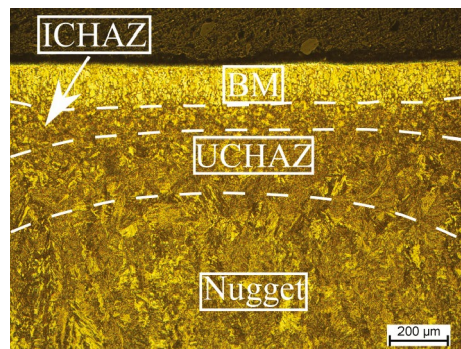
**(a)** Macrostructure of the UFREW joints.



**(b)** Higher magnification of Region A in Figure 4.a.



**(c)** Macrostructure of the DFREW joints.



**(d)** Higher magnification of Region E in Figure 4.c.

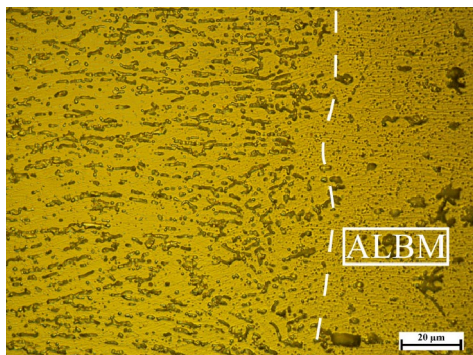
to higher current density and causes severe indentation. The indentation suppresses the rivet. Thus, the widths of BM and ICHAZ at the centerline are relatively smaller compared with those of the UFREW joints. HAZ expands to the sides of the rivet.

Figure 8 presents the scanning electron microscopy (SEM) images of the weld microstructure near the bond line. As shown in Fig. 8a, the steel plate is deformed around the nugget and some gas ducts can be observed due to the heat input and electrode indentation. Notches between the rivet and steel plate can also be seen in

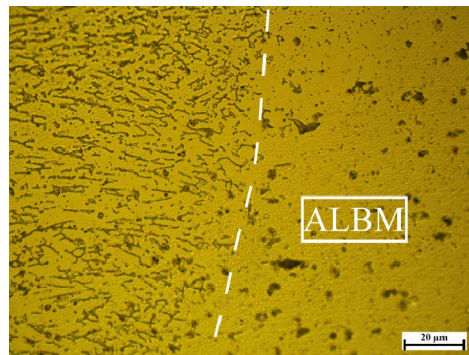
Fig. 8a–c. In Fig. 8d, no gaps can be found between the notches and the nugget because the corona bond is formed to connect the edge of the nugget and the notch root. A similar bond phenomenon of two steel plates was also reported by Ma et al. [21]. Figure 8e shows the energy-dispersive spectroscopy (EDS) map of Fig. 8a. The ferrite (Fe = red) and the Al (red) are sharply separated from each other. We can see Al melted and flow into the notches in Fig. 8e.

Points 1 to 6 in Fig. 8f were examined via EDS to check the chemical compositions of the notches. Table 3 lists

**Fig. 5** Microstructure of the Al nugget of the FREW joints

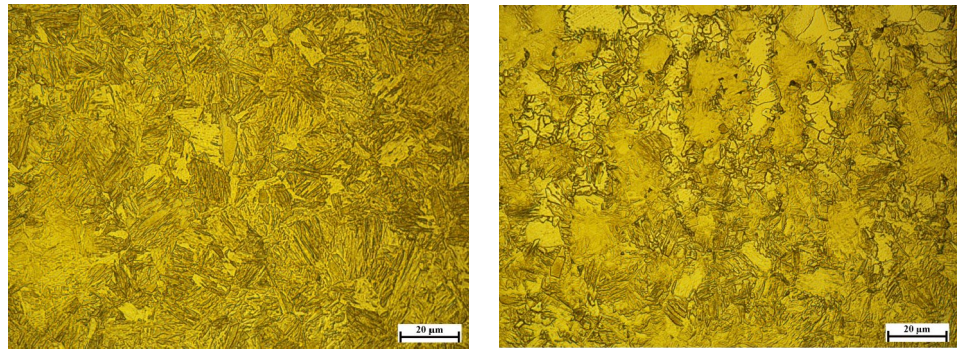
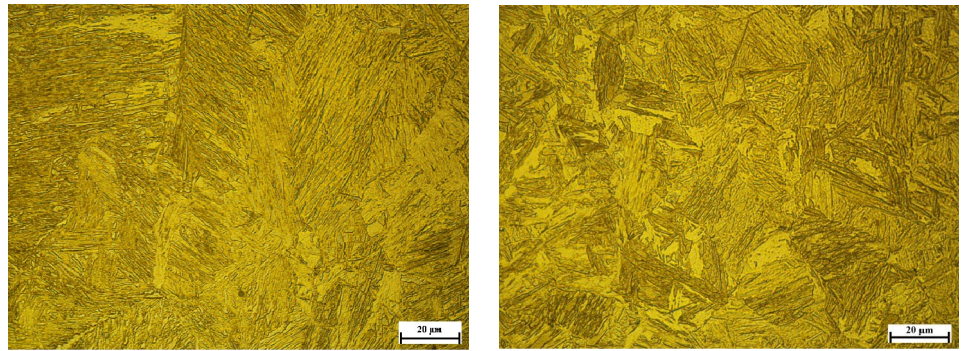


**(a)** Al nugget of the UFREW joints.



**(b)** Al nugget of the DFREW joints.

**Fig. 6** Microstructure of the nugget and HAZ of the rivet

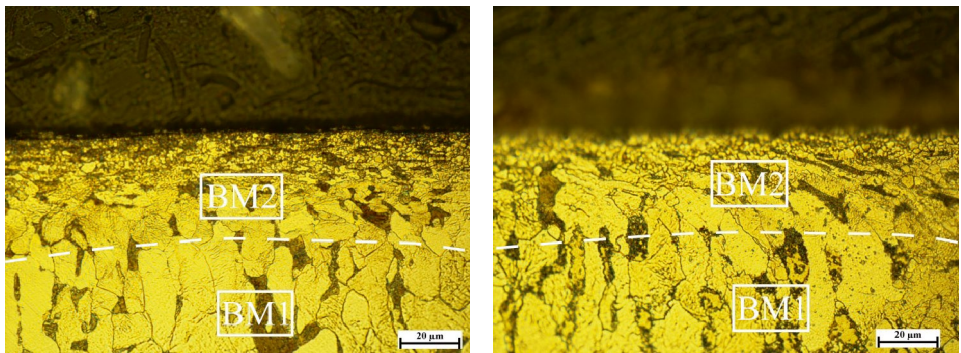


Points 1 to 6 from the SEM images in Fig. 8f. The table includes the weight and atomic percentages of Al and Fe. Points 1 and 6 are on the rivet and steel plate, respectively. Point 6 is closer to the notches, and its Al content of 0.72% is higher than that of Point 1. Al atoms diffuse into steel because Point 1 is closer to the notches. The atomic ratio of Al to Fe of Points 2 to 4 is approximately 7:3, indicating that Fe diffuses into Al melton. However, the proportion of Fe in Point 5 is slightly increased. An assumption can be made that more Fe is diffused because of the proximity of the steel plate.

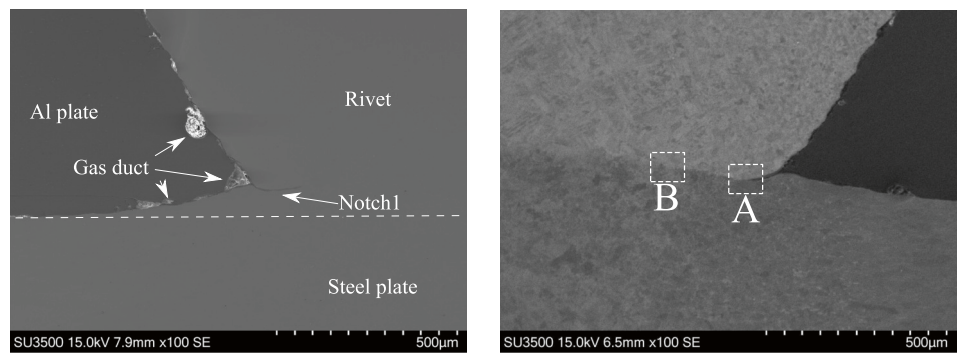
### 3.2 Hardness characteristics

Figure 9a presents the hardness profile of a typical UFREW joint, which is divided into six zones depending on the hardness value. The average hardness of the BM of the rivet is 223.8HV. The average hardness of the rivets ICHAZ and UCHAZ is higher than that of the BM because of the martensitic transformation in HAZ. The material of UCHAZ is exposed to more welding heat during welding. The microstructure of UCHAZ basically consists of larger martensite grains, while the microstructure of ICHAZ consists

**Fig. 7** Microstructure of the BM of the rivet

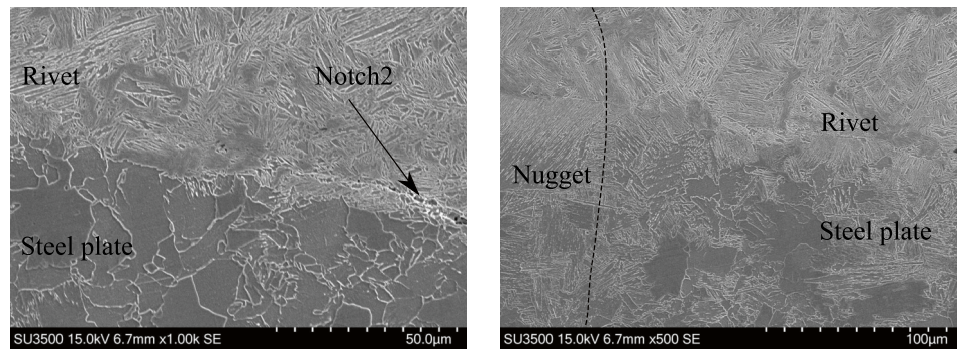


**Fig. 8** The SEM and EDS analysis images of the bond area



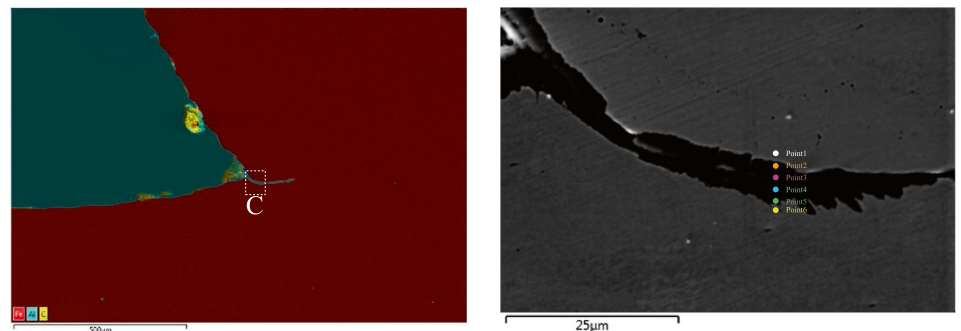
**(a)** SEM image of the bond area between the rivet and steel plate.

**(b)** SEM image of the etched bond area between the rivet and steel plate.



**(c)** Higher magnification of Region A in Figure 8.b.

**(d)** Higher magnification of Region B in Figure 8.b.



**(e)** EDS mapping image of Figure 8.a.

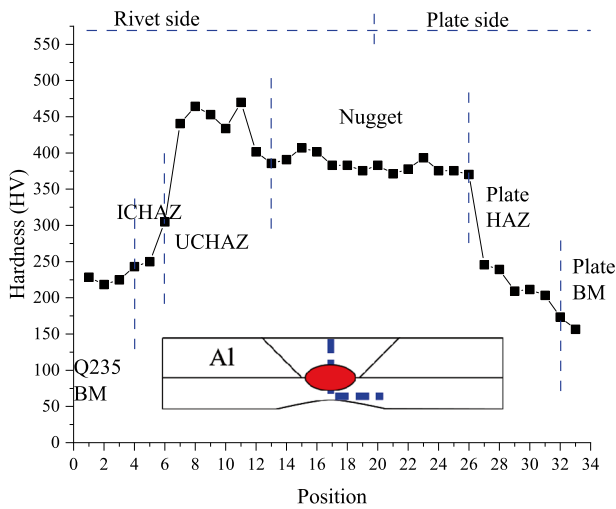
**(f)** Spots for EDS analysis of higher magnification of Region C in Figure 8.e.

**Table 3** Chemical composition at Spots 1 to 6 in Fig. 8f

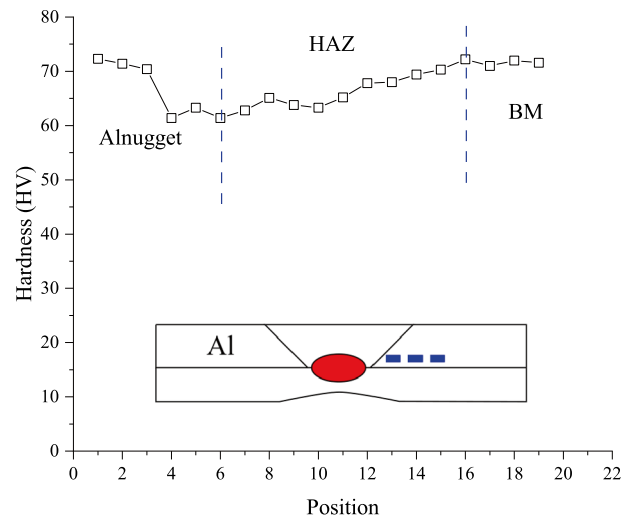
	Weight-%		Atom-%	
	Al-K	Fe-K	Al-K	Fe-K
Point 1	0.00%	100.00%	0.00%	100.00%
Point 2	51.11%	48.89%	68.23%	31.77%
Point 3	53.06%	46.94%	70.06%	29.94%
Point 4	52.14%	47.86%	69.27%	30.73%
Point 5	26.48%	73.52%	42.71%	57.29%
Point 6	0.35%	99.65%	0.72%	99.28%

of martensite and ferrite. Therefore, the average hardness of UCHAZ is higher than that of ICHAZ. The location of peak hardness is inside UCHAZ, close to the nugget, and the microstructure in this region is coarse-grained martensite. The average hardness of the nugget is 386.05HV. The average hardness of the BM of the Q235 plate is 156.65HV.

The hardness profile of the Al side is shown in Fig. 9b, and it can be divided into three zones based on hardness. HAZ has the lowest average hardness because of the influence of welding heat, resulting in the elimination of the



(a) Hardness profile of the center line of the UFREW joints.



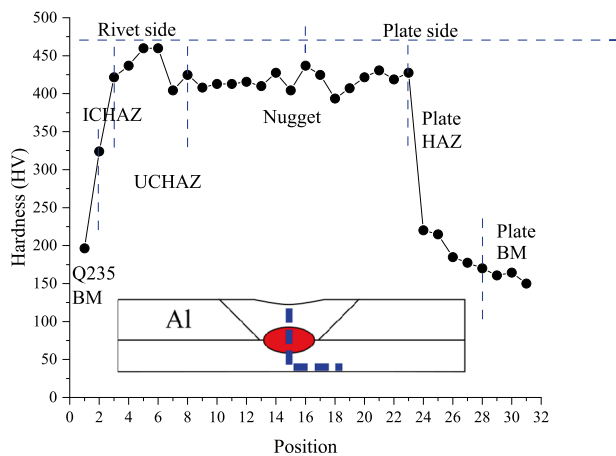
(b) Hardness profile of Al side of the UFREW joints.

Fig. 9 Hardness profile of a typical UFREW joint

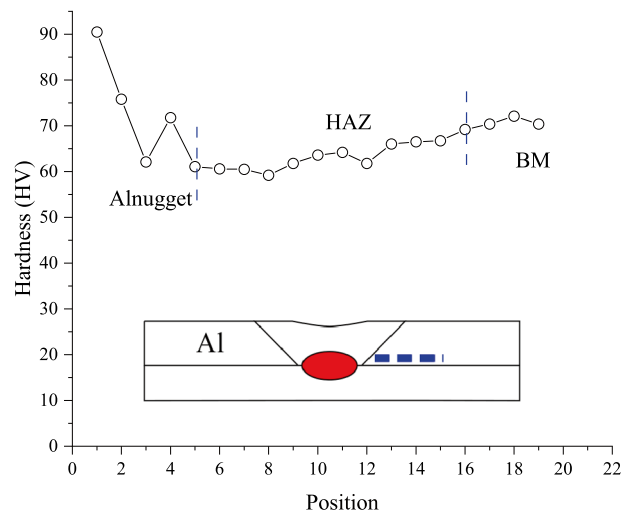
work-hardening effect of the base material and larger grain size. The average hardness of the nugget of the Al plate is higher than that of HAZ, probably due to the formation of fine columnar crystals, as shown in Fig. 5a, b. The BM of aluminum is the hardest, with an average hardness of 70.53HV.

The hardness profile of a typical DFREW joint is shown in Fig. 10. The widths of BM and ICHAZ are relatively small because welding indentation happens on the rivet

side. Hardness is tested on equal space, and thus, the hardness of the BM and ICHAZ of the DFREW joints is tested on only one position, resulting in difficulty in identifying the average hardness of these regions. As shown in Fig. 11, the DFREW joints have higher average hardness in most regions due to the higher welding current and the heat input. The hardness of the plate’s HAZ of the UFREW joints is higher because of the work hardening of the electrode force on the plate side.



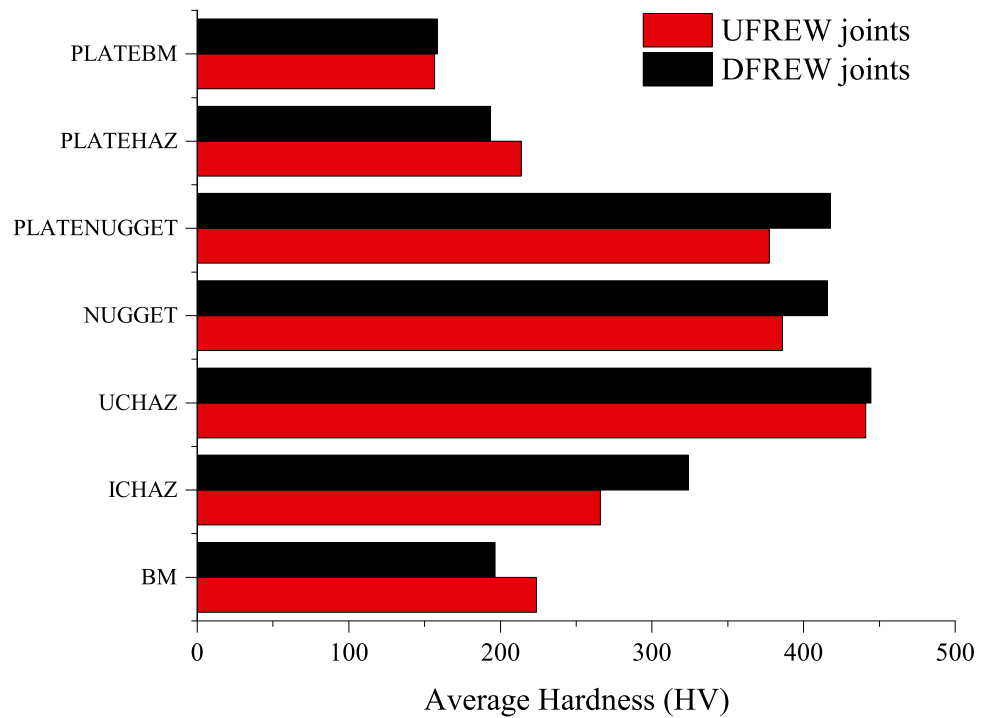
(a) Hardness profile of the center line of the DFREW joints.



(b) Hardness profile of the Al side of the DFREW joints.

Fig. 10 Hardness profile of a typical DFREW joint

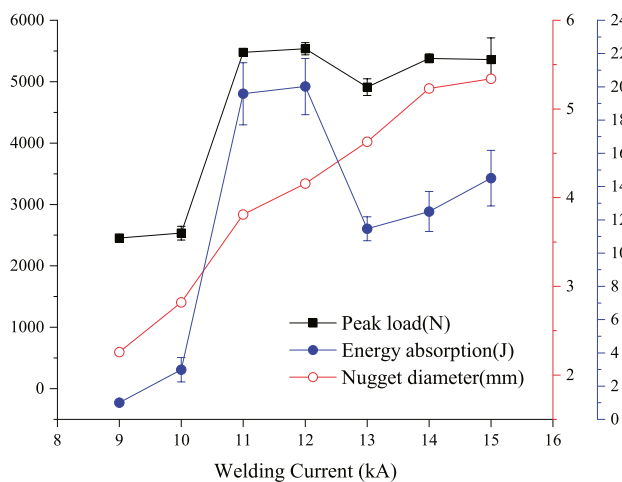
**Fig. 11** Comparison of the average hardness of the UFREW and DFREW joints



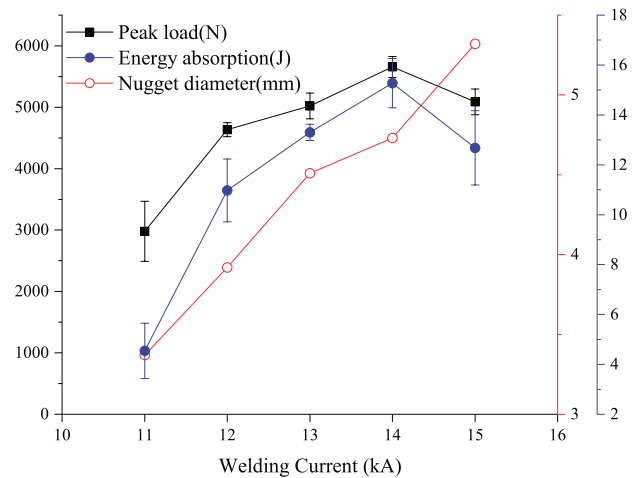
### 3.3 Tensile shear performance

The tensile shear performance of the FREW joints is closely related to nugget size, and welding current exerts a significant effect on nugget diameter. For the UFREW joints, as shown in Fig. 12a, when the welding current increases from 9 to 12 kA, the nugget diameter increases from 2.26 to 4.16 mm, and peak load and energy absorption value increase from 2.45 kN and 1.01 J to 5.54 kN and 20.01 J, respectively. More heat is produced in the welding zone as

the current continues to increase. Although the diameter of the nugget increases with increasing heat input, the HAZ of the plate is also expanding, reducing the hardness of the BM. When the current exceeds 15kA, severe electrode indentation occurs around the joint, and a large amount of melted Al is extruded. Therefore, as pointed out by Xia et al. [22], expulsion and factors, such as porosity and excessive electrode indentation, will cause the degradation of joint strength and collision stability, decreasing the tensile shear performance of the joint.



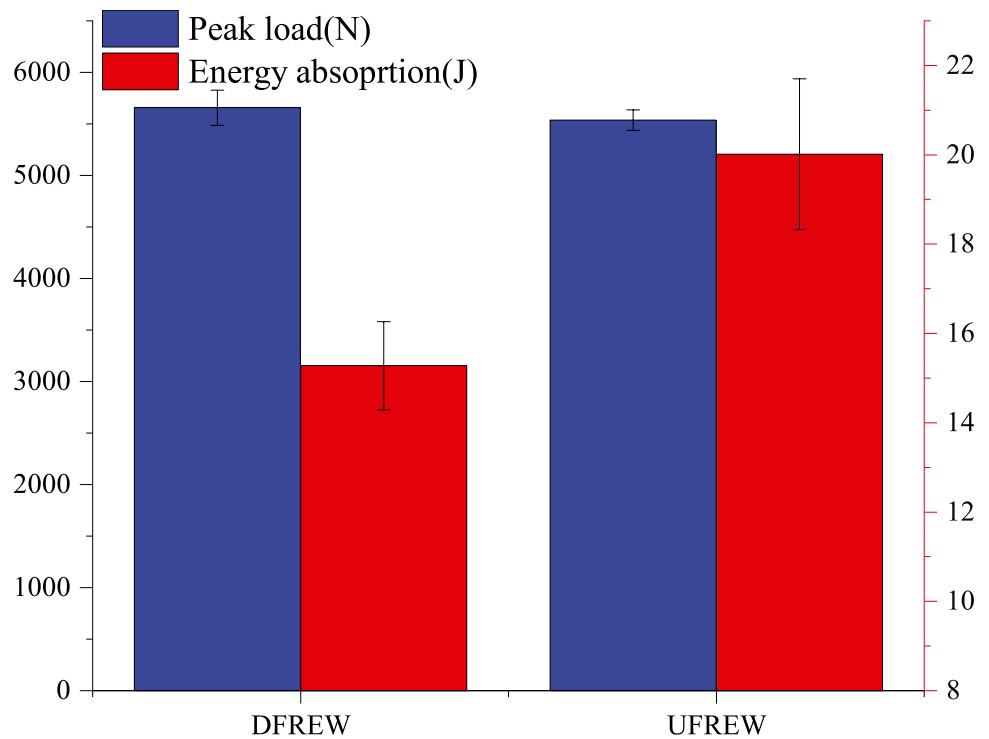
**(a)** UFREW joints.



**(b)** DFREW joints.

**Fig. 12** Peak load, energy absorption and nugget diameter of the UFREW and DFREW joints obtained at different welding currents

**Fig. 13** Comparison of the peak load and energy absorption of the joints obtained using the two methods

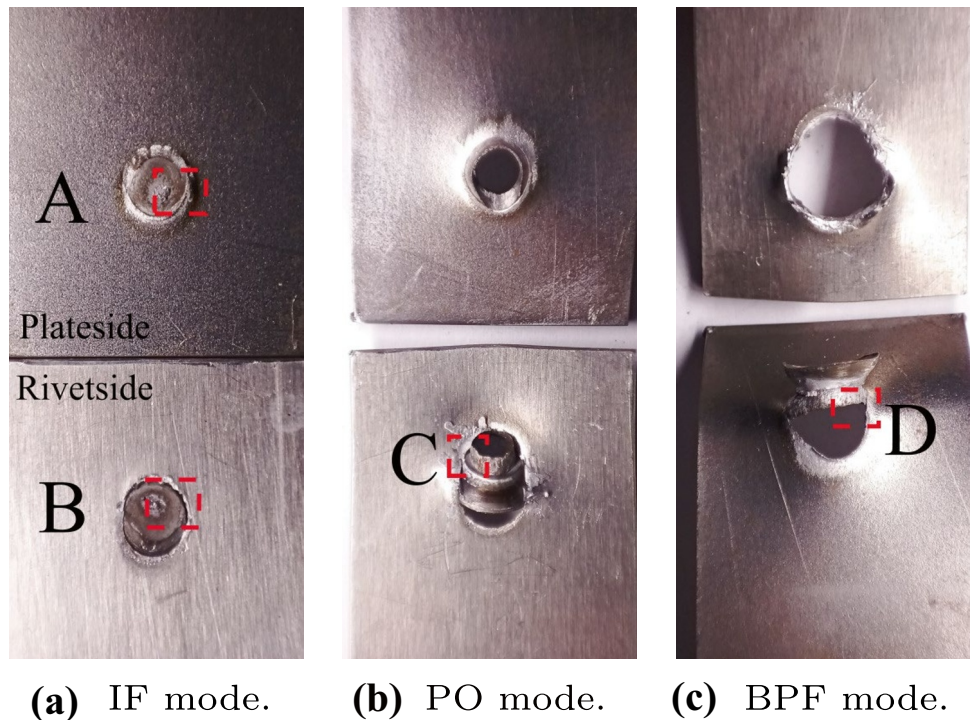


For the DFREW joints, as shown in Fig. 12b, the nugget diameter increases from 3.37 to 4.73 mm when welding current is increased from 11 to 14 kA. The peak load and energy absorption value increase from 2.98 kN and 4.54 J to 5.65 kN and 15.28 J, respectively. As current increases to 16 kA, peak load and energy absorption drop to 5.08 kN

and 12.68 J, respectively, due to electrode indentation and expulsion.

Figure 13 compares the maximum peak load and energy absorption of the two methods. The UFREW joints exhibit superior tensile shear performance. The peak load of the UFREW joints is close to that of the DFREW joints. However,

**Fig. 14** Fracture appearance of the FREW joints



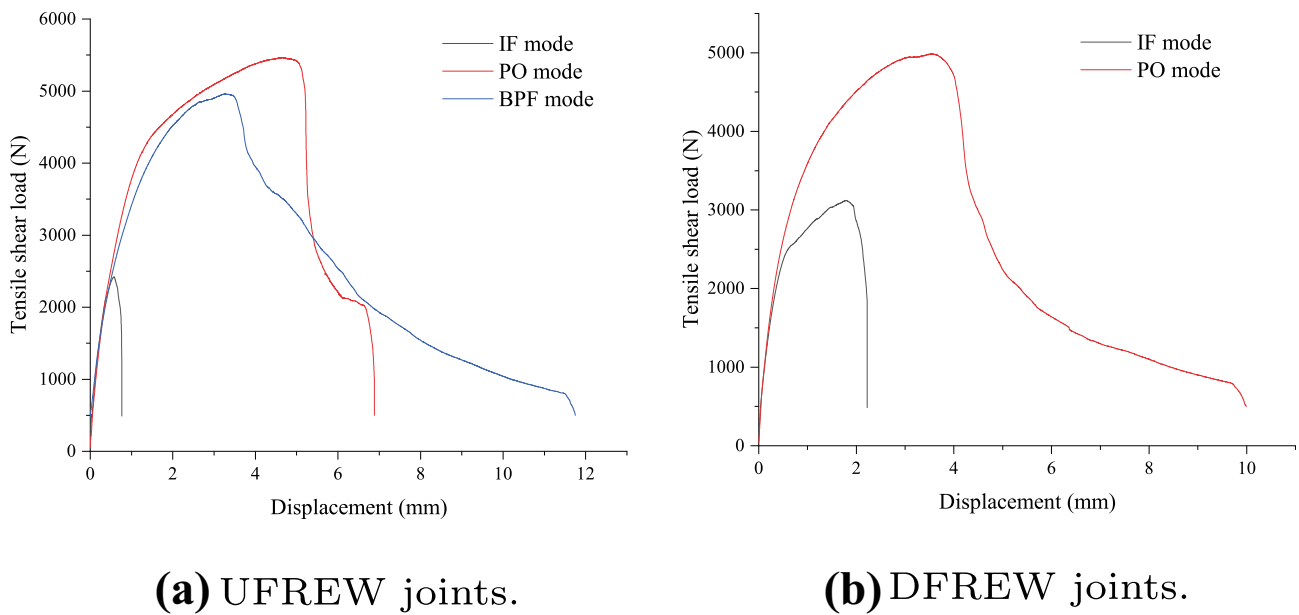
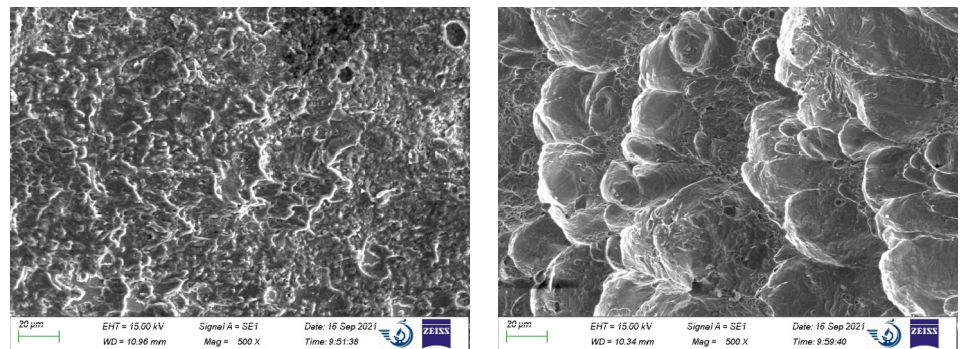


**Fig. 15** Typical tensile shear load curves for joints under different failure mode

to obtain a relatively high peak load (above 4900N), the current ranges required by UFREW and DFREW are 11–15 kA and 13–15 kA, respectively. The UFREW joints required less

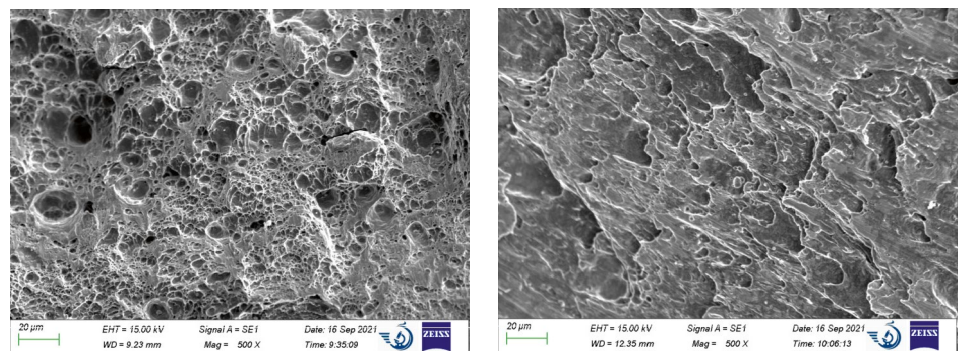
current and larger welding current range. Moreover, the maximum energy absorption value of the UFREW joints is 20.98 J, while that of the DFREW joints is 16.55 J.

**Fig. 16** Fracture surface morphology of the FREW joints



**(a)** Fracture surface morphology of the palte side under IF mode (Region A in Figure 14.a).

**(b)** Fracture surface morphology of the rivet side under IF mode (Region B in Figure 14.a).



**(c)** Fracture surface morphology under PO mode (Region C in Figure 14.b).

**(d)** Fracture surface morphology under BPO mode (Region D in Figure 14.c).

### 3.4 Failure mode

Failure mode is a qualitative measurement of joint performance. Welding current exerts a profound influence on failure mode. As shown in Fig. 14a, when the applied welding current is 9kA and 11kA for UFREW and DFREW, respectively, the nugget is not sufficiently strong to support the tensile shear force, the crack propagates in the direction of the rivet/steel sheet interface through the nugget, and failure mode is interface failure (IF) mode. When the welding current is increased, the crack grows through the periphery of the nugget, and the failure mode changes to pull-out failure (PO) mode, as shown in Fig. 14b. The reason for change in the failure mode is the increasing nugget diameter. Pouranvari [23] reported that with increasing nugget diameter, resistance to IF mode also increases. When the critical nugget diameter is reached, the failure mode changes to PO.

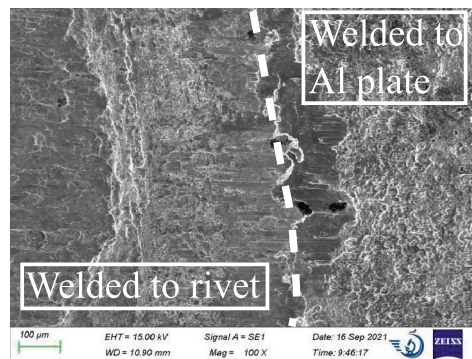
With a further increase in welding current, weld indentation becomes deeper with increasing heat input. For UFREW, the area of the steel plate bearing area decreases, and the rotation of the joint area under tensile shear load becomes larger. After reaching the peak load, part of the material in the steel plate's BM are pulled out with the nugget and failure mode changes to BM pull-out failure (BPF) mode, as shown in Fig. 14c. For DFREW joints, indentation

mostly occurs at the rivet side, and the failure mode remains as PO with increasing current.

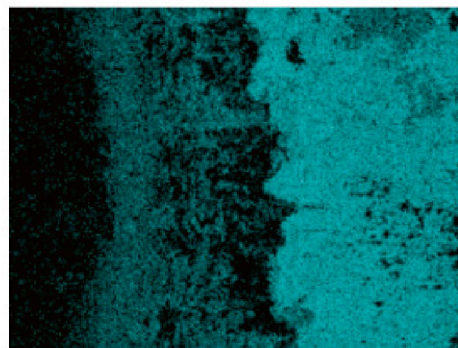
The tensile shear load curves of UFREW and DFREW joints under different failure modes are shown in Fig. 15a, b. As illustrated in Fig. 15, sudden failure occurs after reaching the peak load under IF mode, indicating a brittle fracture with low energy absorption. The curve of PO mode indicates that the joint is plastically deformed while the nugget is being stripped from the BM. For BPF mode, tensile shear load drops slowly after reaching the peak load, and tensile displacement is larger compared with that under PO mode, indicating ductile failure.

The morphology of the fracture surface of the FREW joints under IF mode is shown in Fig. 16a, b, where the fracture surface is filled with smooth planes, indicating brittle fracture. Figure 17 shows the EDS map of the fracture surface of the plate side under IF mode, indicating the presence of Al on the surface of the Q235 plates. This finding further confirms the presence of the brazed joints between Al and Q235. Figure 16c shows the presence of dimples and smooth small planes at the fracture in PO mode, signifying quasi-cleavage fracture. Figure 16d shows the presence of distinctive tear ridges and dimples at the fracture under the BPF mode, indicating ductile fracture.

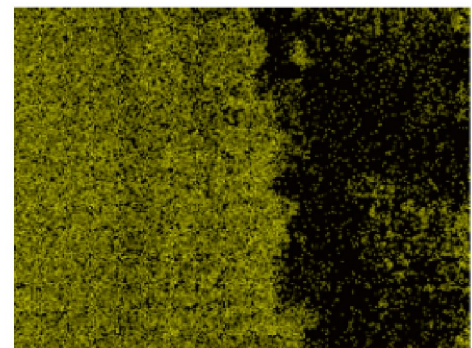
**Fig. 17** EDS mapping of Al and Fe on the fracture surface of the plate side (Region A in Fig. 14a) under IF mode



**(a)** Fracture surface characteristics under IF mode.



**(b)** Distribution of Al.



**(c)** Distribution of Fe.

## 4 Conclusions

FREW was used to join a 2 mm thick 6061 Al alloy and a 1.5 mm thick Q235 steel plate. The process was performed using two methods: UFREW and DFREW. The microstructure and mechanical properties of the joints were analyzed, and the following conclusions were obtained.

1. Nugget diameter increased with rising heat input. The microstructure of the nugget was martensite. HAZ could be divided into UCHAZ and ICHAZ. The microstructure of the former was martensite with a smaller grain size than the nugget, and that of the latter was martensite with ferrite.
2. The UFREW joints exhibited better tensile shear performance than the DFREW joints. The joints obtained using the two processes have similar maximum peak loads, but the maximum energy absorption values of UFREW and DFREW were 20.98 J and 16.55 J, respectively. The UFREW joints achieved greater energy absorption and required lower welding current and larger welding current range.
3. The failure mode of the UFREW joints changed from IF mode to PO, and finally, to BPF mode as current increased. The highest tensile shear load was obtained under PO mode. For DFREW, the failure mode changed from IF mode to PO mode with increasing welding current.

**Abbreviations** REW: Resistance element welding; FREW: Flat resistance element welding; RSW: Resistance spot welding; UFREW: Upward flat resistance element welding; DFREW: Downward flat resistance element welding; IF: Interface failure; PO: Pull-out failure; BPF: Base material pull-out failure; SPR: Self-pierce riveting; BM: Base material; HAZ: Heat-affected zone; UCHAZ: Upper-critical heat-affected zone; ICHAZ: Inter-critical heat-affected zone

**Author contributions** Liangyu Fei and Shengdun Zhao contributed to the study's conception and design. Material preparation and data collection and analysis were performed by Liangyu Fei and Peng Zhang. The first draft of the manuscript was written by Liangyu Fei. Zhiyan Feng, Fei Jiang, and Hao Zhou commented on previous versions of the manuscript.

**Funding** This work was supported by the Joint Fund for Aerospace Advanced Manufacturing Technology Research Key Program (Grant No. U1937203) and the Joint Funds of the Natural Science Foundation of Shaanxi Province (Grant No. 2019JLP-06).

**Availability of data and material** Not applicable.

**Code availability** Not applicable.

## Declarations

**Ethics approval** Not applicable

**Consent to participate** All the authors participated in this research.

**Consent for publication** All the authors approved the final manuscript for publication.

**Conflict of interest** The authors declare no competing interests.

## References

1. Cui X, Wang S, Hu SJ (2008) A method for optimal design of automotive body assembly using multi-material construction. *Materials & Design* 29(2):381–387
2. Feng M-N, Chen Y, Fu D-H, Qu C, Luo Z (2018) Fatigue behaviour and life estimation of Mg/Al ultrasonic spot weld bonding welds. *Sci Technol Weld Joining* 23(6):487–500
3. Kumar A, Sharma G, Dwivedi DK (2018) TIG spot weld bonding of 409 L ferritic stainless steel. *Int J Adhes Adhes* 84:350–359
4. Ramachandran KK, Murugan N, Kumar SS (2015) Effect of tool axis offset and geometry of tool pin profile on the characteristics of friction stir welded dissimilar joints of aluminum alloy AA5052 and HSLA steel. *Materials Science and Engineering a-Structural Materials Properties Microstructure and Processing* 639:219–233
5. Meschut G, Hahn O, Janzen V, Olfermann T (2014) Innovative joining technologies for multi-material structures. *Welding in the World* 58(1):65–75
6. Pouranvari M, Marashi S (2013) Critical review of automotive steels spot welding: process, structure and properties. *Sci Technol Weld Joining* 18(5):361–403
7. Shah LH, Ishak M (2014) Review of research progress on aluminum-steel dissimilar welding. *Mater Manuf Processes* 29(8):928–933
8. Tamizi M, Pouranvari M, Movahedi M (2017) Welding metallurgy of martensitic advanced high strength steels during resistance spot welding. *Sci Technol Weld Joining* 22(4):327–335
9. Xu Y (2006) Effects of factors on physical attributes of self-piercing riveted joints. *Sci Technol Weld Joining* 11(6):666–671
10. Ma Y, Lou M, Li Y, Lin Z (2018) Effect of rivet and die on self-piercing rivetability of AA6061-T6 and mild steel CR4 of different gauges. *J Mater Process Technol* 251:282–294
11. Meschut G, Schmal C, Olfermann T (2017) Process characteristics and load-bearing capacities of joints welded with elements for the application in multi-material design. *Welding in the World* 61(3):435–442
12. Ling ZX, Li Y, Luo Z, Feng YQ, Wang ZM (2016) Resistance element welding of 6061 aluminum alloy to uncoated 22MnMoB boron steel. *Mater Manuf Processes* 31(16):2174–2180
13. Manladan SM, Yusof F, Ramesh S, Zhang Y, Luo Z, Ling Z (2017) Microstructure and mechanical properties of resistance spot welded in welding-brazing mode and resistance element welded magnesium alloy/austenitic stainless steel joints. *J Mater Process Technol* 250:45–54
14. Schmal C, Meschut G (2020) Process characteristics and influences of production-related disturbances in resistance element welding of hybrid materials with steel cover sheets and polymer core. *Welding in the World* 64(3):437–448. <https://doi.org/10.1007/s40194-019-00842-w>

15. Troschitz J, Vorderbrüggen J, Kupfer R, Gude M, Meschut G (2020) Joining of thermoplastic composites with metals using resistance element welding. *Appl Sci* 10(20):7251. <https://doi.org/10.3390/app10207251>
16. Wang S, Li Y, Yang Y, Manladan SM, Luo Z (2021) Resistance element welding of 7075 aluminum alloy to Ti6Al4V titanium alloy. *J Manuf Process* 70:300–306. <https://doi.org/10.1016/j.jmapro.2021.08.047>
17. Wan Z, Wang H-P, Chen N, Wang M, Carlson BE (2017) Characterization of intermetallic compound at the interfaces of al-steel resistance spot welds. *J Mater Process Technol* 242:12–23
18. Chipman J (1972) Thermodynamics and phase diagram of the Fe-C system. *Metall and Mater Trans B* 3(1):55–64
19. Gould J, Khurana S, Li T (2006) Predictions of microstructures when welding automotive advanced high-strength steels. *Welding Journal-New York* 85(5):111
20. Beni SS, Atapour M, Salmani MR, Ashiri R (2019) Resistance spot welding metallurgy of thin sheets of zinc-coated interstitial-free steel. *Metall and Mater Trans A* 50(5):2218–2234
21. Ma Y, Takikawa A, Nakanishi J, Doira K, Shimizu T, Lu Y, Ma N (2021) Measurement of local material properties and failure analysis of resistance spot welds of advanced high-strength steel sheets. *Materials & Design* 201:109505
22. Xia YJ, Su ZW, Li YB, Zhou L, Shen Y (2019) Online quantitative evaluation of expulsion in resistance spot welding. *J Manuf Process* 46:34–43
23. Pouranvari M (2017) Fracture toughness of martensitic stainless steel resistance spot welds. *Materials Science and Engineering a-Structural Materials Properties Microstructure and Processing* 680:97–107

**Publisher's Note** Springer Nature remains neutral with regard to jurisdictional claims in published maps and institutional affiliations.